Optics Letters

# Nonlinear pulse compression based on a gas-filled multipass cell

L. Lavenu,[1,2,*] M. Natile,[3,4] F. Guichard,[2] Y. Zaouter,[2] X. Delen,[1] M. Hanna,[1] E. Mottay,[2] and P. Georges[1]

[1]Laboratoire Charles Fabry, Institut d'Optique Graduate School, CNRS, Université Paris-Saclay, 91127 Palaiseau Cedex, France
[2]Amplitude Systèmes, Cité de la Photonique, 11 avenue de Canteranne, 33600 Pessac, France
[3]Amplitude Technologies, 2-4 rue du bois Chaland, 91029 Evry, France
[4]LIDyL, CEA, CNRS, Université Paris-Saclay, CEA-SACLAY, 91191 Gif-sur-Yvette, France
*Corresponding author: loic.lavenu@institutoptique.fr

Received 23 February 2018; revised 4 April 2018; accepted 5 April 2018; posted 11 April 2018 (Doc. ID 324809); published 4 May 2018

**We demonstrate nonlinear temporal compression of a high-energy Yb-doped fiber laser source in a multipass cell filled with argon. The 160 μJ 275 fs input pulses are compressed down to 135 μJ 33 fs at the output, corresponding to an overall transmission of 85%. We also analyze the output beam, revealing essentially no space-time couplings. We believe this technique can be scalable to higher pulse energies and shorter pulse durations, enabling access to a wider parameter range for a large variety of ultrafast laser sources.** 

***OCIS codes:*** (320.7110) Ultrafast nonlinear optics; (320.5520) Pulse compression; (320.7090) Ultrafast lasers.

https://doi.org/10.1364/OL.43.002252

Nonlinear pulse compression is a well-known technique to reduce the pulse duration of ultrafast laser sources. In particular, this technique allows us to reach the few-cycle regime either from Ti:Sa lasers [1,2] or Yb-doped fiber laser sources [3,4]. It consists of imparting spectral broadening by propagation through a Kerr medium and compensating for the induced frequency chirp by a controlled amount of group delay dispersion. Depending on the laser input peak power, different nonlinear media may be used. For high peak power (typically above 300 MW), the most commonly used nonlinear medium is a gas-filled capillary [1–5]. This allows the generation of high spatial quality output beams. The limitations of this technique are related to the fact that the guided modes exhibit propagation losses and require keeping the capillaries perfectly straight. Experimentally, the capillary core diameter is usually larger than 250 μm to achieve fundamental mode transmission per stage higher than 50% [3–5]. Then, to ensure a large compression factor, >1 m length capillaries are preferred, resulting in large footprint setups. Alternatively, stretched fiber has been used successfully to realize both the energy scaling and improve the efficiency of capillary-based post-compression. However, the improvements come at the expense of very long devices [6,7].

To overcome the drawbacks of the above-mentioned techniques, some experiments use bulk media to broaden the spectrum [8–10]. Nevertheless, the broadening factor is limited in these setups because the spatial Kerr effect typically has a strong impact on the beam quality and induces spatio-temporal couplings.

Recently, a new scheme for nonlinear compression has been proposed and implemented [11,12]. In this scheme, the setup is composed of a multipass cell that incorporates a nonlinear bulk medium. Several experiments [12–14], as well as numerical simulations [15], show that if the *B*-integral per pass in the medium is sufficiently small, propagation in the cell homogenizes the spectrum over the beam transverse dimensions, even if the peak power exceeds the critical power for self-focusing in the medium. This technique has allowed temporal compression of 10–50 MW input peak power pulses, where capillaries lack efficiency due to the small inner core dimension required. This technique also allows remarkable overall transmissions (up to 90%) at an average power of several hundred watts.

In Ref. [15], we proposed to use a multipass cell filled with gas as the broadening medium and showed through numerical simulations that the spatial homogenizing effect can still occur. This allows us to retain the advantages of the multipass cell, notably the robustness to beam pointing fluctuations and high transmission, which permit access to larger pulse energies and facilitate dispersion management in the cell. Instead of being accumulated in a discrete manner at each pass through the nonlinear medium, the *B*-integral increases continuously. In this case, the peak power must remain below the critical power, which can be made arbitrarily large by reducing the gas pressure.

In this Letter, we experimentally demonstrate this technique for the first time, to the best of our knowledge, using a high-energy Yb-doped fiber source delivering 160 μJ 275 fs pulses at a 150 kHz repetition rate. These parameters correspond to an input peak power of 485 MW, which is 10 times higher than previous experiments. Propagation in the argon-filled multipass cell and subsequent compression results in 135 μJ 33 fs output pulses, corresponding to a compression factor of 8.3. We

相比于入射光的性质来说

analyze the output beam quality and spatio-temporal couplings, and, in excellent agreement with numerical simulations, find that the beam is essentially homogeneous at the output. Therefore, we believe that this technique will open the range of parameters accessible with ultrafast sources, most notably Ti:Sa- and Yb-based systems.

The experimental setup, shown in Fig. 1, starts with a high-energy Yb-doped fiber amplifier [16] delivering 160 μJ pulses at a central wavelength of 1030 nm and at a 150 kHz repetition rate, corresponding to an average power of 24 W. The pulse duration is 275 fs, corresponding to an input peak power of 485 MW, as shown in Fig. 1. The output spatial beam quality is close to the diffraction limit, with measured $M^2$ values of 1.15 × 1.15 along two orthogonal axes.

In order to decrease the pulse duration of the laser, the beam is sent into a gas-filled multipass cell composed of two 2 in diameter concave mirrors with a radius of curvature of 300 mm incorporated into a pressurized chamber filled with 7 bars of argon. This gas pressure results in a nonlinear index $n_2 = 6.5 \times 10^{-23}$ $m^2/W$ and a group velocity dispersion $\beta_2 = 110$ $fs^2/m$ [17]. The corresponding critical power for self-focusing is 2 GW, roughly four times the input peak power. Coupling in and out of the multipass cell is done using rectangular 3 × 10 $mm^2$ mirrors located in front of one of the concave mirrors. All mirrors are coated to ensure low group delay dispersion ($|GDD| < 20$ $fs^2$) and a high reflection coefficient (> 99.5%) on a 910–1180 nm bandwidth. The distance between concave mirrors is chosen to be 280 mm, close to the confocal configuration. The number of roundtrips through the cavity can be adjusted by finely tuning the cell length. In this experiment, the beam was aligned to propagate through 34 roundtrips, resulting in a distance between the mirrors of 286.5 mm and an overall propagation length, including the path before and after the cavity in the gas cell of 20.9 m. The resonant waist radius, to which the input beam is mode matched within 5% width, is 220 μm at the cavity center, expanding to 300 μm on the concave mirrors. The multipass cell chamber is sealed using a 1 in diameter, 5 mm thick AR-coated calcium fluoride windows. The total footprint of the pressure

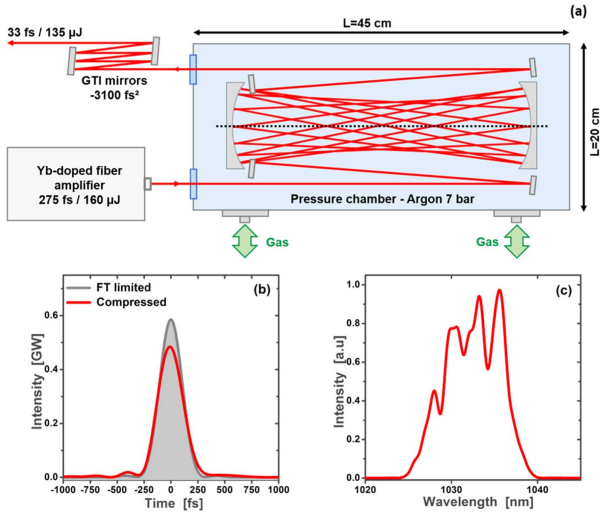


**Fig. 1.** (a) Experimental setup. (b) Pulse profile at the output of the laser (red) and Fourier-transform-limited profile (gray) corresponding to the spectrum shown in (c).

chamber is 45 cm × 20 cm. At the output of the cell, the beam is collimated and sent to the compressor composed of a pair of dispersive mirrors with −250 $fs^2$ GDD coating and a second pair of mirrors with −100 $fs^2$ GDD coating on a 980–1080 nm bandwidth. The total introduced dispersion at the compressor is −3100 $fs^2$.

The power transmission of the cavity, measured between the input and output of the pressure chamber, is 93%. The total transmission of the setup, including the mode-matching optics and compressor mirrors, is 85%. This transmission is constant as the input power is increased from 0 to 24 W. During propagation in the cell, the spatially averaged *B*-integral per roundtrip obtained using the analytical estimate from [15] is 0.6 rad. In these experimental conditions, the effect of gas dispersion, corresponding to 60 $fs^2$ per roundtrip, is not negligible, and results in a pulse width measured at the output of the cavity of 550 fs. This decreases the spectral broadening, and the total *B*-integral estimated using numerical simulations is 14.9 rad. This effect also limits the compression ratio achievable with the setup as described in Ref. [18], and the compensation of the gas dispersion using engineered concave mirror coatings could be used to allow further pulse compression. As shown in Fig. 2, the pulse at the output of the cavity exhibits a 93 nm spectral bandwidth at −10 dB, corresponding to a Fourier transform-limited pulse duration of 31 fs. The compressed pulse is characterized using a home-built second-harmonic generation frequency resolved optical gating (FROG) setup. The results are plotted on Fig. 2. The FROG error is $33 \times 10^{-4}$ over a grid size of 512 × 512. The retrieved spectrum and autocorrelation are compared to independent measurements, showing excellent agreement. The peak power and fraction of energy in the main temporal lobe inferred from the FROG measurement are 3.25 GW and 82%, respectively, corresponding to a peak power enhancement factor of 6.7. The spectral and temporal profiles obtained using the numerical model described in Ref. [15], where the input condition is the FROG-measured input laser pulse, and compression is achieved using pure quadratic spectral phase, are shown in Fig. 2 and are in quantitative agreement with the measured data.

Figure 2 also shows the measured long-term stability of the setup in terms of pulse duration and average power over 24 h. The RMS deviation of the power is 0.3%. The pulse duration stability is within 2 fs peak-to-peak (1.1 fs RMS). These measurements highlight the long-term robustness of the setup.

An important question in multipass cell-based compression setups is the spatial beam quality and spatio-spectral couplings in the output beam. Figure 3 shows the $M^2$ measurement performed at maximum energy on the compressed beam, giving a value of 1.15 × 1.25. The ellipticity of the output beam is 0.93. The collimated beam profile after the compressor is shown in the inset. The beam quality over two orthogonal axes is also measured as a function of input energy, in the presence or absence of gas, in order to identify respective contributions from the input laser, cavity optics, and filling gas. It is clear that in our experimental conditions, the multipass cell setup preserves the beam quality. The beam quality is slightly different in the horizontal and vertical direction, which might be due to a small misalignment in the mode-matching optics.

We then study the spatio-spectral couplings in the beam after compression using a spectro-imaging setup. The beam size is first reduced by a factor of 4 using a telescope. It is then sent

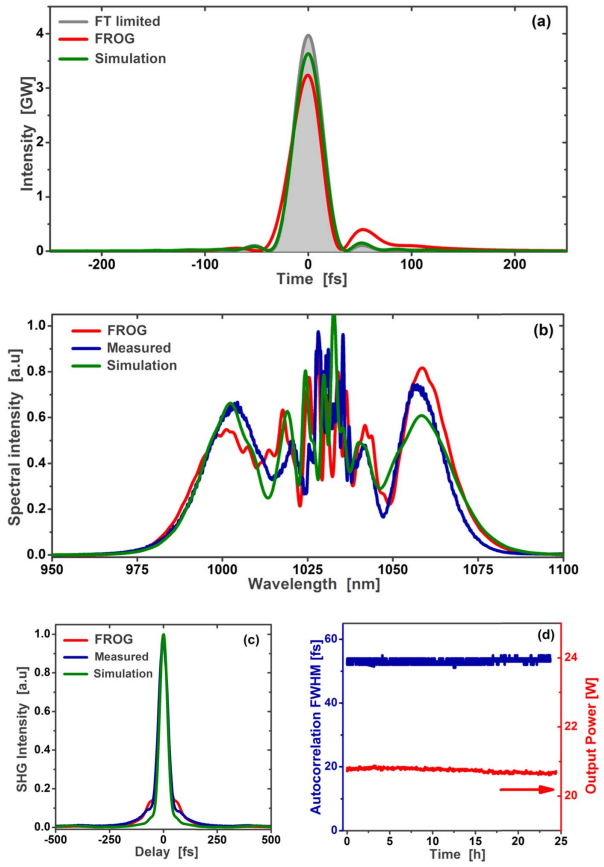


**Fig. 2.** Characterization of the compressed pulse at the output of the cavity for 160 μJ input energy with 85% transmission corresponding to 135 μJ output pulse energy and 20 W average power. (a) FROG-retrieved pulse intensity profile (red), Fourier transform-limited profile of the FROG-retrieved spectrum (gray), and simulated pulse profile (green). (b) FROG-retrieved spectrum (red) compared to an independently measured spectrum (blue) and simulated spectrum (green). (c) FROG-retrieved autocorrelation (red) compared to independently measured autocorrelation (blue) and simulated autocorrelation (green). (d) Autocorrelation FWHM and average power stability over 24 h.

to an $f$-$f$ arrangement composed of a 500 line/mm grating, a 75 mm lens, and a CCD camera with a 4 μm pixel size. The $1/e^2$ beam diameter at the camera in the nonspectrally resolved axis is 200 μm, which corresponds to 50 pixels on the camera.

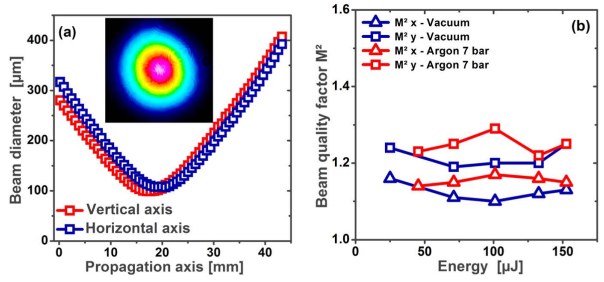


**Fig. 3.** Beam quality at the output of the cavity. (a) $M^2$ measurement at maximum energy. Inset: output beam profile. (b) Output $M^2$ as a function of input energy in vacuum (blue) and 7 bars of argon (red).

On the spectrally resolved axis, the spectral resolution is 5 nm. The spatio-spectral profile for the vertical axis displayed on the camera is shown in Fig. 4, along with the result obtained from the numerical simulation. Both are in good agreement and show essentially no spatio-spectral coupling in the output beam. The central structure at 1030 nm is not resolved by the spectro-imaging setup. In addition, note that the reduced intensity observed at long wavelengths on the measured spatio-spectral field is due to the decreasing sensitivity of the Si-based camera. The horizontal axis is measured by rotating the beam by 90°, yielding essentially the same result. This data can be used to compute the spectral overlap integral V between any location in the beam and the beam center, as defined in Ref. [13]. The result is plotted in Fig. 4 for both the vertical and horizontal directions. The overlap is above 93% at locations in the beam where the intensity is above 10% of the beam center. Below, the overlap integral is degraded, but remains above 80%. This decay is mainly due to the reduced signal-to-noise ratio in this intensity range. However, the mean overlap, obtained by computing the first moment of V over the beam, is 99.0% for the horizontal axis and 99.3% for the vertical axis, confirming that the output beam is essentially free of spatio-spectral couplings, as expected in the simulation where the mean overlap is 99.9%.

Finally, we perform several measurements to investigate the setup robustness and reliability. Table 1 compares the results of

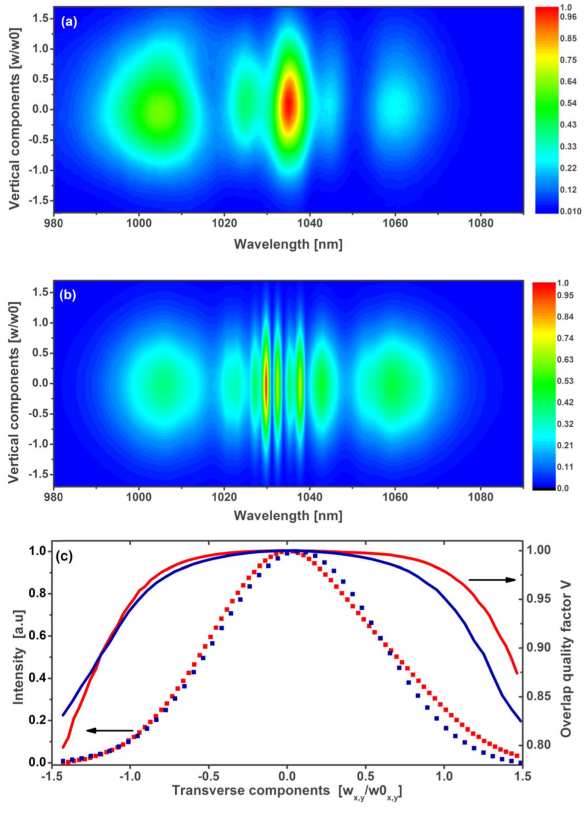


**Fig. 4.** Spatio-spectral couplings at the output of the cavity in the vertical axis. (a) Experimental spectro-imaging measurement. (b) Simulated spectro-imaging measurement. (c) Spatio-spectral quality factor measured with a spectro-imaging setup: vertical axis (red), horizontal axis (blue).

**Table 1. Parameters at the Laser and Multipass Cell Output**

| Quantity | Unit | Laser | Cell |
|---|---|---|---|
| $\Delta\tau$ | fs | 275 | 33 |
| $E$ | μJ | 160 | 135 |
| $P_{peak}$ | MW | 485 | 3250 |
| $P2P_{RMS}$ | % | 1.13 | 1.2 |
| $\sigma_{RMS}$ | % | 0.14 | 0.3 |
| $\Delta\tau_{RMS}$ | % | — | 1.1 |
| PER | dB | 30 | 22.8 |
| $\langle M^2\rangle$ | — | 1.15 | 1.2 |
| $\theta_{RMS}$ | μrad | 10 | 10 |

measurements made directly at the laser output and at the output of the multipass cell on the compressed pulse at maximum energy. These measurements include FWHM pulse duration ($\Delta\tau$), energy ($E$), peak intensity ($P_{PEAK}$), pulse-to-pulse (short-term) energy stability ($P2P_{RMS}$), long-term energy stability ($\sigma_{RMS}$), and long-term pulse duration stability ($\Delta\tau_{RMS}$) over 24 h, a polarization extinction ratio (PER), beam quality averaged over both axes ($\langle M^2\rangle$), and angular beam pointing stability ($\theta_{RMS}$). Again, the data show that the use of a multipass cell is very promising, since pulse duration is efficiently reduced, and peak power is scaled accordingly, while the other input laser characteristics are mostly preserved by the compression setup.

In this setup, the limitation on input pulse energy is related to the damage fluence of the mirror, 130 $mJ/cm^2$, corresponding to an input pulse energy of 200 μJ. However, as described in Ref. [15], this limitation can be addressed by using higher damage threshold mirrors and by scaling the cavity geometry to obtain larger beam diameters at the mirrors. Numerical simulations suggest that meter-sized cavities should allow input pulse energies in the 10–500 mJ range, depending on the exact damage threshold. In terms of attainable pulse duration, the limitations are mostly technical and related to the dispersion management and spectral bandwidth of the mirror coatings. In the current state of mirror coating technology, we see no obstacle to compressing pulses down to the few-cycle regime. Finally, as far as pulse compression ratio is concerned, the limitations are the maximum gas pressure allowable before the onset of spatio-temporal couplings, which depends on the cavity configuration, the number of roundtrips achievable in a particular implementation, and the implementation of gas dispersion compensation using the mirror coatings. Numerical simulations performed in Ref. [15] show that a compression ratio of 15 should be achievable.

To conclude, we demonstrate the nonlinear compression of an Yb-doped fiber laser ultrafast amplifier using a gas-filled multipass cell. This technique allows the production of 33 fs, 135 μJ, and 3250 MW pulses which are the shortest pulses reported after a mutipass cell-based compression setup to date. Compared to capillaries, gas-filled multipass cells allow very efficient compression, longer propagation distances, and larger beam sizes. Moreover, progress in mirror coating technologies, with a damage threshold increasing over the years [19] and dispersion management capabilities over broader bandwidths [20], suggests that this technique could be used advantageously in a large number of ultrafast laser systems. The overall agreement between our experimental data with a 3D numerical model describing the propagation is excellent, including the absence of spatio-temporal couplings. This highlights the fact that spatio-temporal effects at play are well understood. Future works will focus on average power and energy scaling with pulse durations in the few-cycle regime.

**Funding.** Agence Nationale de la Recherche (ANR) (ANR-10-LABX-0039-PALM, ANR-16-CE30-0027-01); Conseil Départemental de l'Essonne (sophie).

## REFERENCES

1. M. Nisoli, S. De Silvestri, O. Svelto, R. Szipöcs, K. Ferencz, Ch. Spielmann, S. Sartania, and F. Krausz, Opt. Lett. **22**, 522 (1997).
2. X. Chen, A. Jullien, A. Malvache, L. Canova, A. Borot, A. Trisorio, C. G. Durfee, and R. Lopez-Martens, Opt. Lett. **34**, 1588 (2009).
3. J. Rothhardt, S. Hädrich, A. Klenke, S. Demmler, A. Hoffmann, T. Gotschall, T. Eidam, M. Krebs, J. Limpert, and A. Tünnermann, Opt. Lett. **39**, 5224 (2014).
4. S. Hädrich, M. Kienel, M. Müller, A. Klenke, J. Rothhardt, R. Klas, T. Gottschall, T. Eidam, A. Drozdy, P. Jójárt, Z. Várallyay, E. Cormier, K. Osvay, A. Tünnermann, and J. Limpert, Opt. Lett. **41**, 4332 (2016).
5. L. Lavenu, M. Natile, F. Guichard, Y. Zaouter, M. Hanna, E. Mottay, and P. Georges, Opt. Express **25**, 7530 (2017).
6. F. Böhle, M. Kretschmar, A. Julien, M. Kovacs, M. Miranda, R. Romero, H. Crespo, U. Morgner, P. Simon, R. Lopez-Martens, and T. Nagy, Laser Phys. Lett. **11**, 095401 (2014).
7. G. Fan, T. Balčiūnas, T. Kanai, T. Flöry, G. Andriukaitis, B. E. Schmidt, F. Légaré, and A. Baltuška, Optica **3**, 1308 (2016).
8. X. Liu, L. Qian, and F. Wise, Opt. Lett. **24**, 1777 (1999).
9. M. Seidel, J. Brons, G. Arisholm, K. Fritsch, V. Pervak, and O. Pronin, Sci. Rep. **7**, 1410 (2017).
10. B. Chen, M. Kretschmar, D. Ehberger, A. Blumenstein, P. Simon, P. Baum, and T. Nagy, Opt. Express **26**, 3861 (2018).
11. N. V. Vysotina, N. N. Rosanov, and V. E. Yashin, Opt. Spectrosc. **110**, 973 (2011).
12. J. Schulte, T. Sartorius, J. Weitenberg, A. Vernaleken, and P. Russbueldt, Opt. Lett. **41**, 4511 (2016).
13. J. Weitenberg, A. Vernaleken, J. Schulte, A. Ozawa, T. Sartorius, V. Pervak, H. Hoffmann, T. Udem, P. Russbüldt, and T. Hänsch, Opt. Express **25**, 20502 (2017).
14. J. Weitenberg, T. Saule, J. Schulte, and P. Rußbüldt, IEEE J. Quantum Electron. **53**, 1 (2017).
15. M. Hanna, X. Délen, L. Lavenu, F. Guichard, Y. Zaouter, F. Druon, and P. Georges, J. Opt. Soc. Am. B **34**, 1340 (2017).
16. Y. Zaouter, J. Boullet, E. Mottay, and E. Cormier, Opt. Lett. **33**, 1527 (2008).
17. C. Bree, A. Demircan, and G. Steinmeyer, IEEE J. Quantum Electron. **46**, 433 (2010).
18. W. J. Tomlinson, R. H. Stolen, and C. V. Shank, J. Opt. Soc. Am. B **1**, 139 (1984).
19. T. Tolensis, L. Grinevičiūtė, L. Smalakys, M. Ščiuka, R. Drazdys, L. Mažulė, R. Buzelis, and A. Melninkaitis, Sci. Rep. **7**, 10898 (2017).
20. N. Lilienfein, C. Hofer, S. Holzberger, C. Matzer, P. Zimmermann, M. Trubetskov, V. Pervak, and I. Pupeza, Opt. Lett. **42**, 271 (2017).